Efficient Perovskite Solar Cells by Metal Ion Doping

SUPLEMENTARY INFORMATION

Experimental

Microstrain analysis (modified Williamson-Hall method)

Both the peak position (*d* spacing) and the full width at half-maximum (FWHM) were determined using a Gaussian fit of the diffracted intensity. The profiles of the observed peak width (Δd_{obs}) of XRD peaks are the results of convoluted functions with multiple effects of instrument response (Δd_{ins}), grain size (Δd_{size}) and microstrain (Δd_{ε}), where we can obtain, equation (1), $\Delta d^2_{obs} = \Delta d^2_{ins} + \Delta d^2_{size} + \Delta d^2_{\varepsilon}$. The Δd_{ins} is the peak width at a stress-free state, usually referring to the instrument contribution. The strain, $\varepsilon = \Delta d_{\varepsilon}/d)$ directly reveals the deformation of the crystal lattice for the specific d_{hkl} plane at a certain stress level. Hence, by rewriting equation (1), we can further obtain equation (2), $\varepsilon = \Delta d_{\varepsilon}/d = (\Delta d^2_{obs} - \Delta d^2_{ins})^{1/2}/d$. Herein, the microstrain can be derived from the slope ε of the $(\Delta d^2_{obs} - \Delta d^2_{ins})^{1/2}$ of the versus *d* plot. We note that using this approach, the microstrain can be derived from the slope of the plot correctly, while to obtain the precise grain size would need a further modification to the current method) as the interception usually present a rather large error and does not work well for grain size larger than micrometre (observed in our films).[1,2]

SEM

The morphologies of the perovskites were investigated using a scanning electron microscopy (SEM) (Hitachi S-4300) at an accelerating voltage of 5kV after platinum coating samples prepared on glass substrates.

Transmission Electron Microscopy (TEM)

The preparation of a cross-sectional lamellar specimen was carried out on a FEI Helios dual beam FEG SEM/FIB microscope, fitted with an Omniprobe micromanipulator for *in-situ* lift-out. The sample preparation was performed following a standard FIB *in-situ* lift-out technique,[3] and the thinning step of the lamellar specimen was performed with decreasing beam current to reduce sample damage and improve sputtering of the material. The cross-sectional specimen was analyzed through high angle annular dark field STEM (HAADF-STEM), using a Fischione detector on a FEI Tecnai Orisis TEM/STEM equipped with a field-assisted thermionic emitter gun, operating at 200 kV.[3]

X-ray diffraction

Diffraction patterns were obtained from samples of perovskite deposited on FTO glass using an X-ray diffractometer (Panalytical X'Pert Pro).

Solar cell characterization

Current-voltage characteristics of the solar cells were measured under AM1.5 light at 100 W/cm^2 generated using an ABET Class AAB sun 2000 simulator calibrated using a National Renewable Energy Laboratories (NREL) calibrated KG5 filtered silicon reference cell, with a 6.5% mismatch factor. Current–voltage curves were measured at a scan rate of 0.38 Vs^{-1} with a

Keithley 2400 sourceMeter. All devices were masked with a 0.0965 cm^2 metal aperture to define the active area and to eliminate edge effects.

Photoluminescence spectroscopy

Perovskite samples were prepared on glass and coated with an inert polymer poly(methyl-methacrylate), PMMA. PL spectra were acquired following previous report[4] using a time-resolved single photon-counting set-up (FluoTime 300, PicoQuant). Samples were photoexcited using a 507-nm laser head (LDH-P-C-510, PicoQuant) with pulse duration of 117 ps, fluence of ~30 nJ/cm^2 per pulse and a repetition rate of 1 MHz. Photolumnincense Quantum Efficiency (PLQE), Steady-state photoluminescence quantum efficiency values were determined using a 532 nm CW laser excitation source (Suwtech LDC-800) to illuminate a sample in an integrating sphere (Oriel Instruments 70682NS), and the laser scatter and PL were collected using a fiber-coupled detector (Ocean Optics MayaPro). The spectral response of the fiber-coupled detector setup was calibrated using a spectral irradiance standard (Oriel Instruments 63358). PLQE calculations were carried out using a homemade established technique.[5]

X-ray and ultra-violet photoemission spectroscopy (XPS and UPS) measurements

Samples for photoemission spectroscopy measurements were transferred to the ultrahigh vacuum chamber (ESCALAB 250Xi) for XPS/UPS measurements. XPS measurements were carried out using a XR6 monochromated Al Kα source (hν = 1486.6 eV) and pass energy of 20 eV. UPS measurements were performed using a He discharge lamp (hν = 21.2 eV) and pass energy of 2 eV.

Nanoscale secondary ion mass spectrometry

A CAMECA NanoSIMS 50 instrument was used to acquire chemical distributions with spatial resolution better than ~100 nm. The instrument uses a 16 keV primary $^{133}Cs^{+}$ beam to bombard the sample surface and collects and analyses selected secondary negative ions. For this experiment, c.a. 300 nm perovskite films were prepared on silicon wafer surfaces. $^{27}Al^{16}O^{-}$ secondary ions were collected to show the distribution of aluminium in the perovskite layer using a D1=3 or 4 aperture to achieve good lateral resolution, and the secondary electron image from the same location. This data is presented over areas of 8 by 8 μm containing 256 by 256 pixels, and was collected without preliminary $^{133}Cs^{+}$ implantation to avoid sputtering away the thin samples. A series of up to 30 sequential images were recorded at the same location to effectively depth profile the sample down to the silicon substrate, and to allow us to locate the centre of the perovskite film from the secondary electron images where the polycrystalline grain structure can be clearly identified. The images were processed using OpenMIMS software (MIMS, Harvard University; www.nrims.harvard.edu).

Atomic force microscopy (AFM)

AFM images were in non-contact mode with perovskite samples prepared on the FTO substrate using a ThermoMicroscopes AutoProbe M5 housed in an acoustic isolation enclosure, with a scan rate of 0.3 Hz and 256 × 256 pixels. We used Aluminum coated antimony doped Si tips (Bruker), which have typical tip radii of 8 nm, resonant frequencies of 75 kHz, and stiffness of 3 N/m.

Inductively coupled plasma optical emission spectrometry (ICP-OES)

A SPECTROBLUE SOP system (Ametek Inc) was utilized for the trace Al^{3+} doping level analysis. Basically, multi-element calibration standard solutions were prepared by diluting the commercial standard solution (100 μg/L, GNM-M33198-2013) with 2% nitric acid in deionized water, giving the final concentrations of 0, 0.05, 0.1, 0.2, 0.5, 1, 2, 5 and 10 μg/L. The ICP-OES analysis was then performed on these calibration standards to obtain the reference peak intensities for Al (167.078 nm) and Pb (220.353 nm). Calibration curves (R2=0.999) were then generated based on these reference peak intensities. After that, the control and the 0.15 mol% Al^{3+} doped film were first dissolved in 2% HNO_3 solution and then tested by ICP-OES system to obtain the Al and Pb signal intensities. By comparing the signal intensities to the calibration standard curves, the contents of Al and Pb could be determined with an error of +-2%, which mainly induced by preparing the standard reference solution.

UV-vis

The absorbance analysis of the perovskite films were deposit on cleaned glasses and measured on a Varian Carry 300 Bio (Agilent Technologies). To minimize any potential errors, at least three samples were determined and the average of all spectra presented.

Fluorescence Microscopy

Optical microscopy and spectroscopy were performed using a custom sample scanning confocal microscope built around a Nikon TE-2000 inverted microscope fitted with an infinity corrected 50x dry objective (Nikon L Plan, NA 0.7, CC 0-1.2). We measured the point spread function of our systems to be ~ 350 nm FWHM. A 470 nm pulsed diode laser (PDL-800 LDH-P-C-470B, 70 ps pulse width), fluence of ~ 30 nJ cm^{-2} per pulse was used for excitation with repetition rate of 40 MHz for collecting fluorescence images. The emission was filtered through a 50/50 dichroic beamsplitter and a 700 nm longpass filter. Photoluminescence from the sample was directed to a Micro Photon Devices (MPD) PDM Series single photon avalanche photodiode with a 50 μm active area. The sample stage was controlled using a piezo controller (Physik Instrumente E-710). For fluorescence images, the pixel step size was set to 100 nm with a pixel dwell time (integration time) of 50 ms.

Kelvin probe and Surface Photo Voltage (SPV)

Vibrating Kelvin Probe (probe diameter = 2 mm, KP Technology, UK) was used to determine the surface potential. All the measurements were done in the ambient condition. Calibration of the kelvin probe was done by a freshly cleaved highly ordered pyrolytic graphite surface which has known work function of 4.65 eV.[6] For SPV measurement, a quartz tungsten halogen lamp was used as a light source and the sample was illuminated from the air interface using an optical fiber coupled to the light source. The intensity was varied linearly by controlling the power supplied to the lamp. The maximum power density on the sample surface was 1mW/cm^2.

External Quantum Efficiency

External quantum efficiency measurements where performed using a modified Bruker Vertex 80 Fourier Transform Infrared spectrometer, coupled to a transimpedance amplifier (Stanford Research SR570). All devices were measured in short circuit configuration under illumination of AM1.5 light at 100 W/cm^2. EQE values were calibrated using a National Renewable Energy Laboratories (NREL) calibrated silicon reference cell with a known EQE spectrum.

Urbach energy

Urbach energies were determined by performing EQE measurements as described above, except with the AM1.5 light source replaced by a tungsten halogen lamp that was filtered with RG715 and KG3 filters. The low energy tail of the measured EQE onset was then fitted using the expression

$$\eta(h\nu) = \eta_0 e^{(h\nu - E_0)/E_{\mathrm{Urbach}}}$$

where $\eta(h\nu)$ is the EQE spectrum, $h\nu$ is the photon energy and E_{Urbach} is the Urbach energy. Weighting factors: A nonlinear regression was performed using MATLAB to extract the Urbach energy from the EQE data. Robust fitting was performed using a bisquared (Tukey's biweight) weighting function. The errors in the Urbach energy based on this fitting procedure represent a 95% confidence limits.

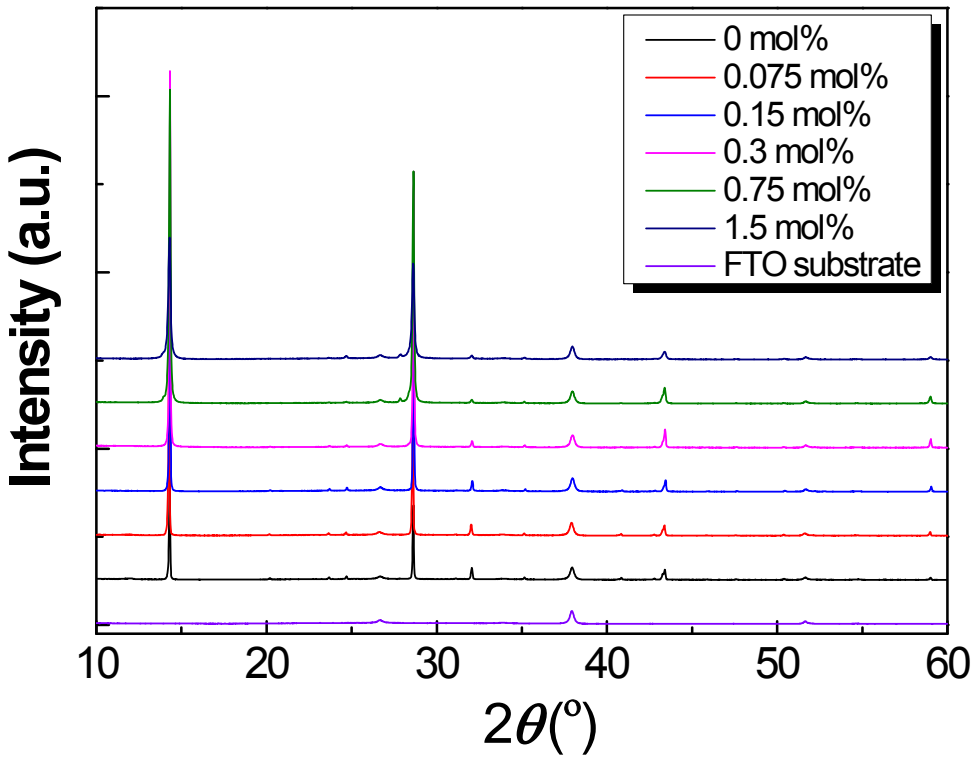

Figure S1. X-ray diffraction patterns analysis of perovskite with different Al^{3+} doping concentration.

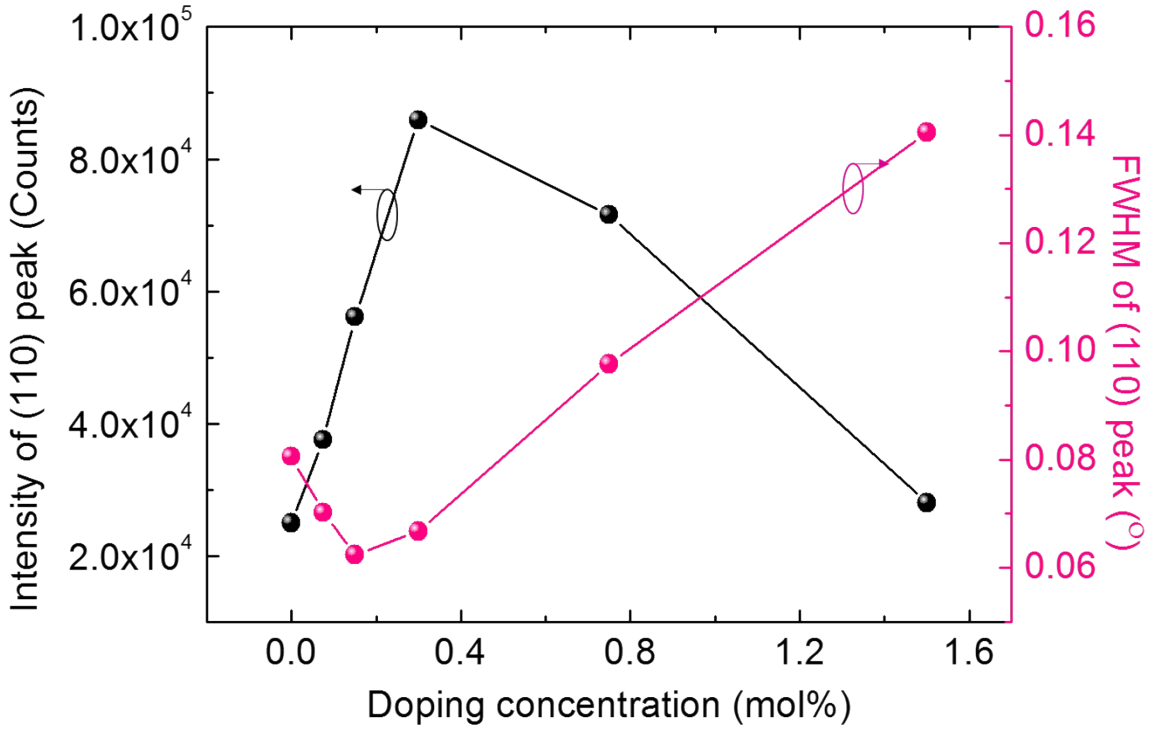

Figure S2. Intensity and FWHM variations of (110) peak with different Al^{3+} doping concentrations.

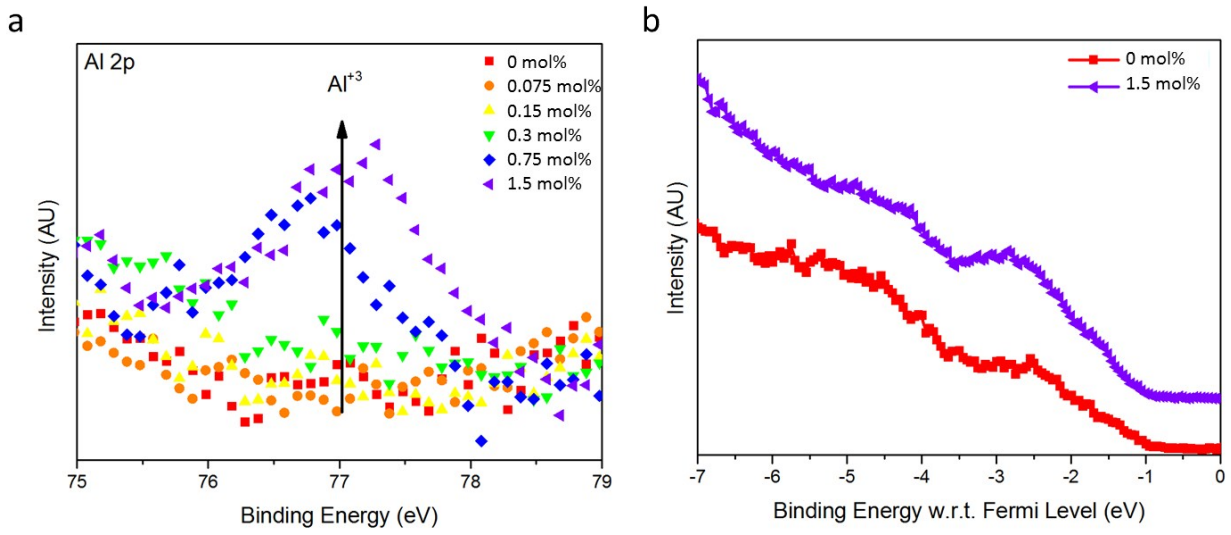

Figure S3. X-ray photoemission spectroscopy (XPS) spectra of Al2p region of control and Al^{3+} doped perovskite films.

In order to give more information about the incorporation of Al^{3+} ions in the films, we performed X-ray photoelectron spectroscopy (XPS), the results of which we show in fig. S3. Due to the closely spaced spin-orbit components for Al2p (Δ = ~ 0.5 eV), we observe a single peak at a binding energy of ~ 77 eV. This high binding energy is in agreement with a +3 oxidation state of Al, as observed previously for Al_2O_3[7] and AlF_3.[8] However, we could not detect the presence of Al^{3+} below 0.3 mol%, due to the concentration falling below the detection level of the instrument.[9]

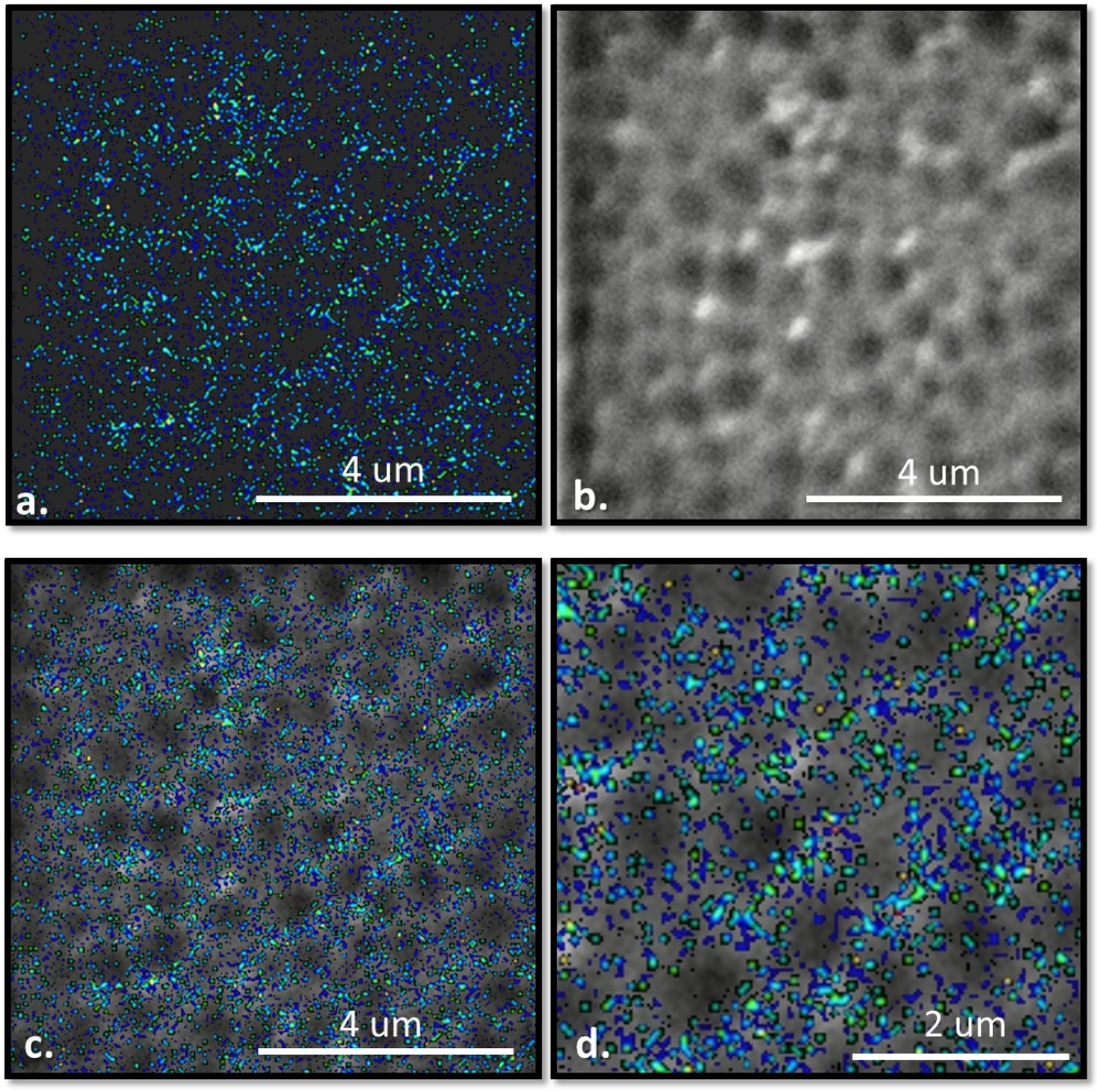

Figure S4. (a) NanoSIMS images showing the AlO^- ions mapping of Al^{3+} -doped (0.15 mol%) perovskite, and (b) their secondary electron image at the same location, where the brighter regions corresponding to the grain boundaries; while (c) displaying the overlap image of a and b, and its enlarged image in (d).

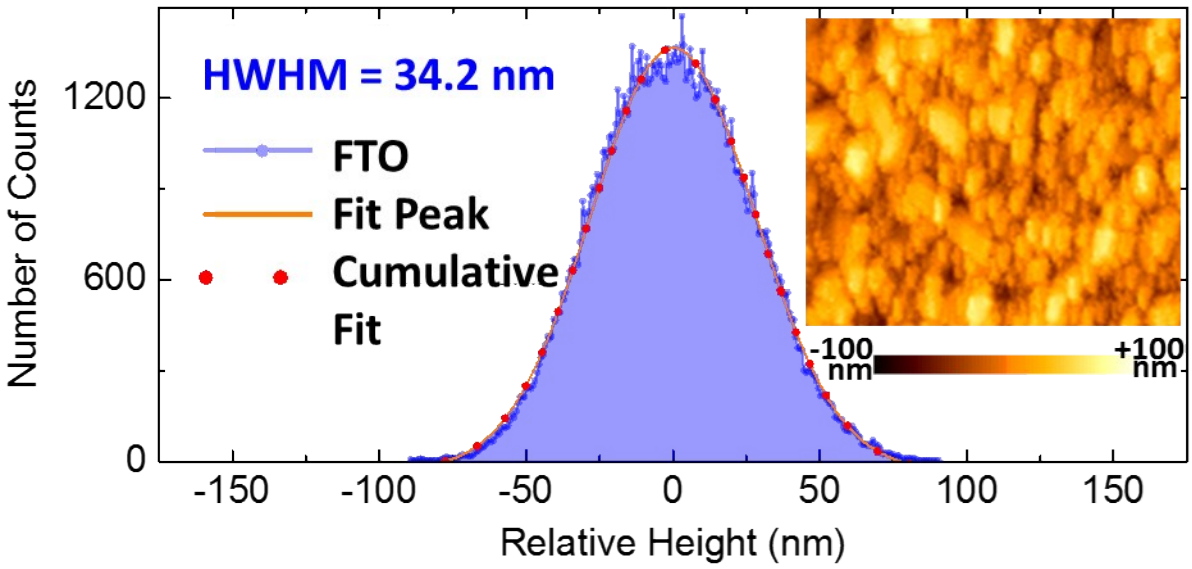

Figure S5. The Atomic Force Microscopy (AFM) image of FTO substrate, where the estimated half-width at half-maximum (HWHM) height distribution is ~34 nm.

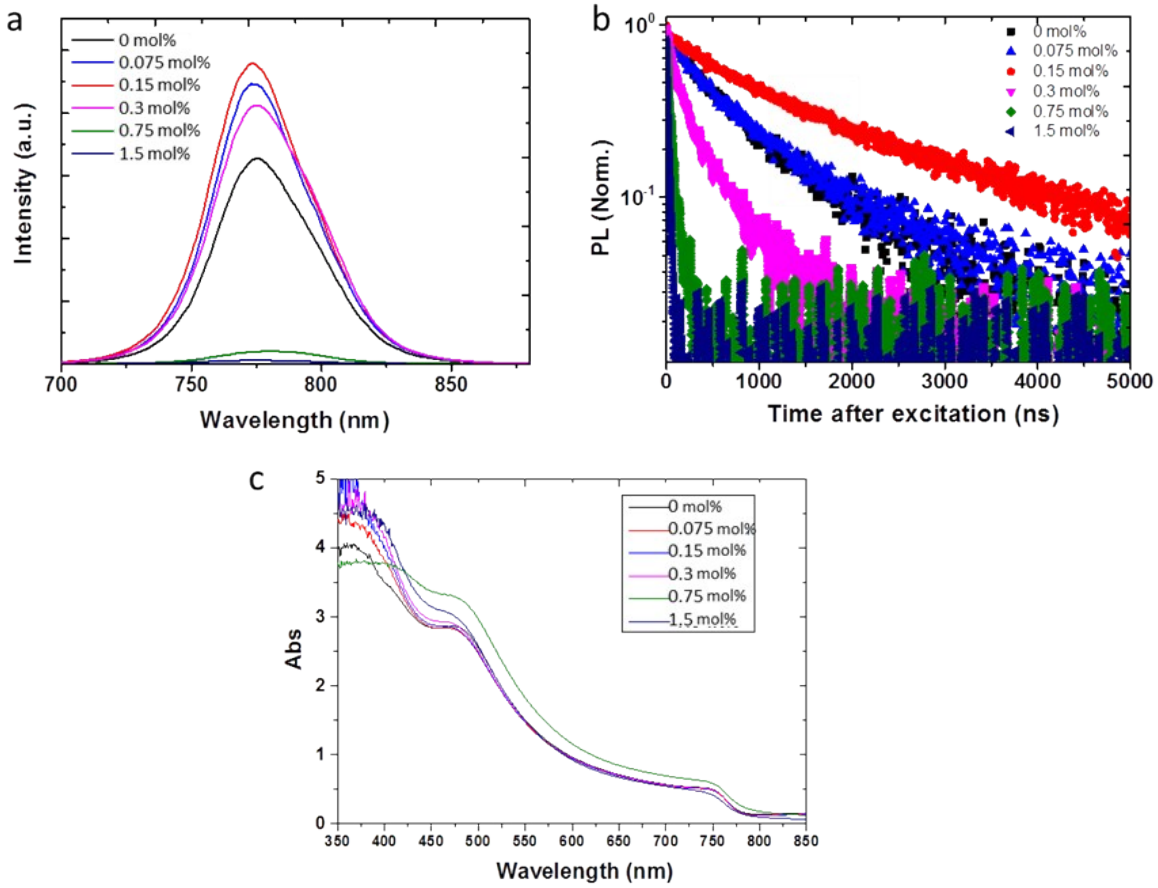

Figure S6. Characterizations of different Al^{3+} doping concentration of perovskite samples with **a)** steady-state photoluminescence, **b)** Time-resolved Photoluminescence decay, **c)** UV-vis absorption spectra.

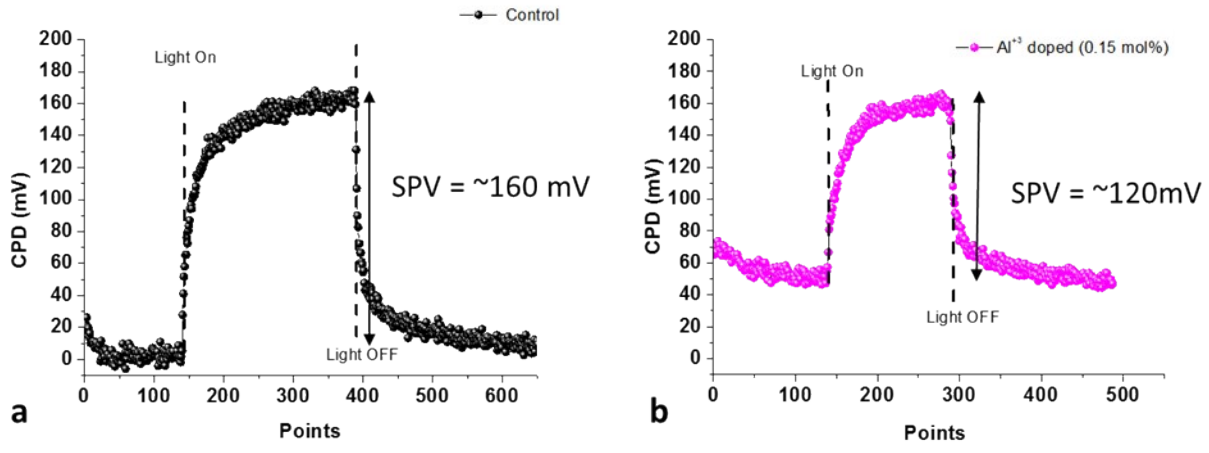

Figure S7: Kelvin probe measurement of a) control and b) doped perovskite films. The dark CPD (contact potential difference) value of the control sample is presented as the reference where the surface work function is 4.80eV The SPV (surface photo voltage) for the doped samples are lower than that of the control sample

In order to understand the effect of Al^{3+} on the energetics of the film surface which comes in contact with the charge transporting layer during the device fabrication, we performed Kelvin probe measurement of perovskite films on FTO in the dark and under illumination.[10] The difference in the work function in the dark and under illumination provides surface photo-voltage, which indicates the degree of band bending at the surface. The band bending at the surface depends on the density of trap states on that surface.[11] We observe in the dark, that the surface work function of a 0.15 mol% Al^{3+}-doped film is higher than that of the control films and the surface photo-voltage of the Al^{3+}-doped films is lower than that of the control. Both the dark and light measurement suggest that there is a shift in the surface potential caused by the Al^{3+} doping, and that the band bending at the surface of Al^{3+}-doped perovskite is lower than that of the control samples. This is consistent with fewer electronic trap sites on surface of the Al^{3+}-doped films.

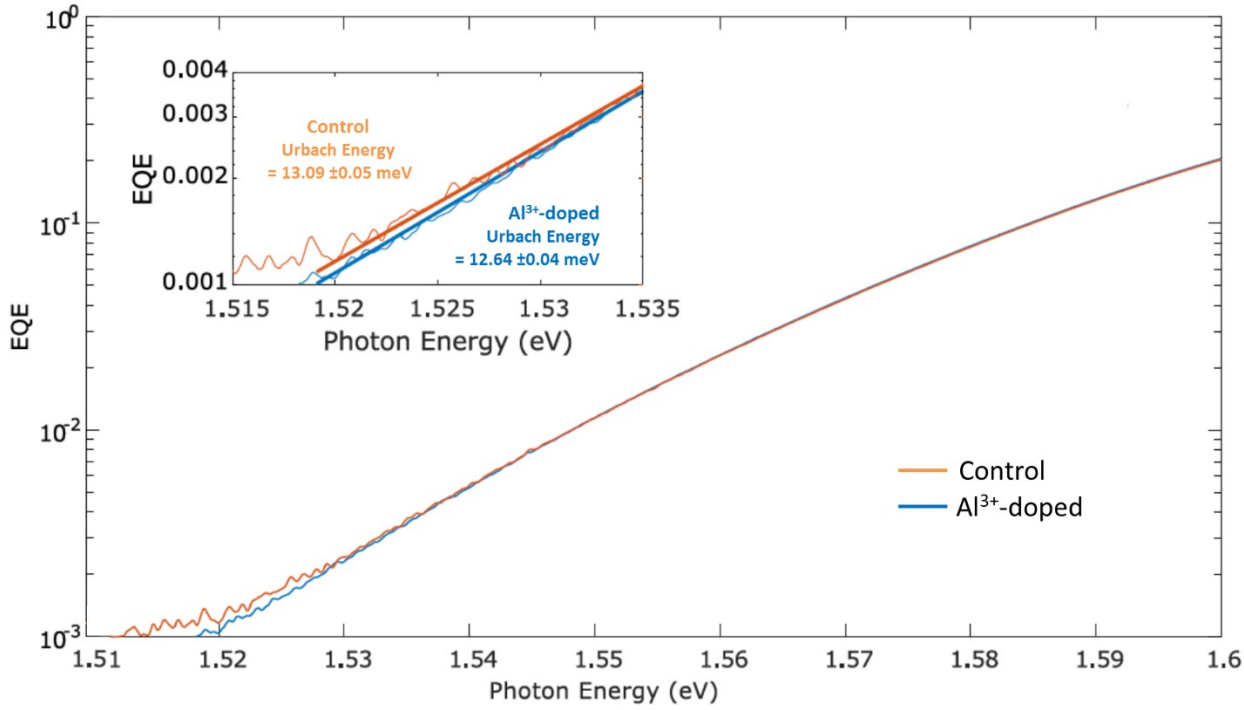

Figure S8. Fourier transform photocurrent spectroscopy of control and Al^{3+}-doped (0.15 mol%) perovskite devices and their estimated Urbach energies fitting the slope at low energy (fits are between 1.519 to 1.55 eV shown in the inlet figure).

A direct method to probe the sub band gap absorption in a photovoltaic device is to make very sensitive measure of the spectral response of the photocurrent via Fourier transform photocurrent spectroscopy (FTPS) on complete solar cells. In an approximation, a shallow slope in the rise in the external quantum efficiency (EQE) below the band gap indicates a large density of sub band gap states, and in contrast a steep rise in the EQE below the band gap indicates a lower density of sub band gap states. We can quantify this steepness, by fitting the exponential rise in the EQE spectra below the band gap, known as the Urbach tail, to derive the Urbach energy (E_u).[12,13] Though the Urbach energy difference between the control and 0.15 mol% Al^{3+}-

doped samples seems small, but this energy difference is corresponding to the low energy states in the trap density, where the small variations in trap density could have a huge impact on device performance.[14,15]

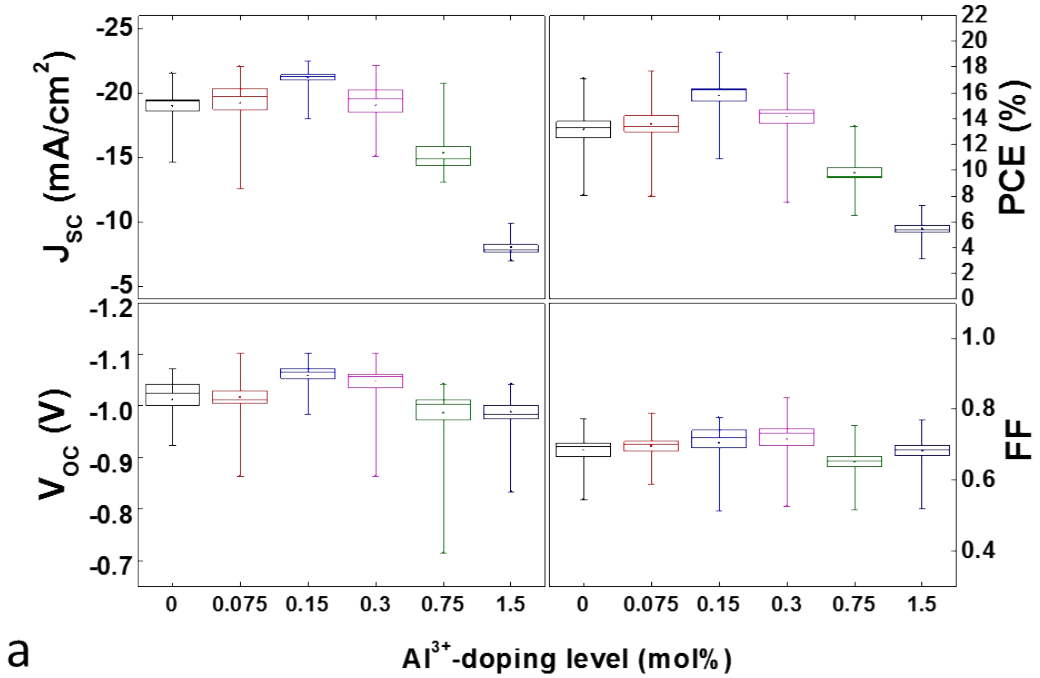

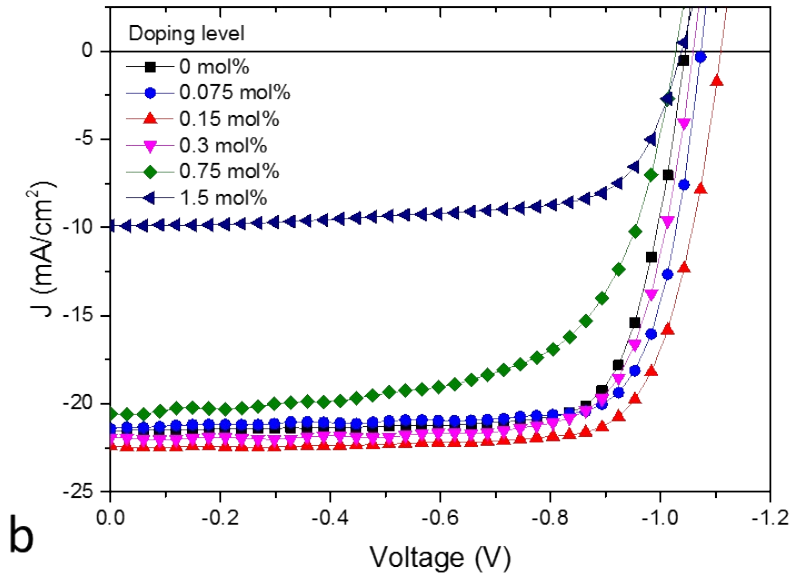

Figure S9: Devices performance characteristics with different doping levels of Al^{3+} perovskite under simulated AM 1.5, 100 mW/cm^2 irradiance in air. **a)** Device performance parameters

extracted from a batch of current-voltage measurements. **b)** The current density-voltage curves of the best devices.

Table S1. Mean solar cell performance parameters with different Al^{3+} doping concentration under simulated AM 1.5, 100 mW/cm^2 solar irradiation.

Doping level (mol%)	J_{sc} (mA/ cm^2)	V_{oc} (V)	FF	PCE (%)
0	19.0±1.7	1.01±0.04	0.68±0.08	13.2±2.6
0.075	19.2±2.4	1.02±0.05	0.70±0.06	13.6±2.8
0.15	21.2±1.1	1.06±0.03	0.71±0.07	15.8±2.4
0.3	19.0±2.4	1.05±0.06	0.72±0.08	14.2±2.4
0.75	15.3±2.4	0.99±0.08	0.65±0.07	9.8±1.9
1.5	8.0±1.0	0.99±0.06	0.68±0.07	5.5±1.2

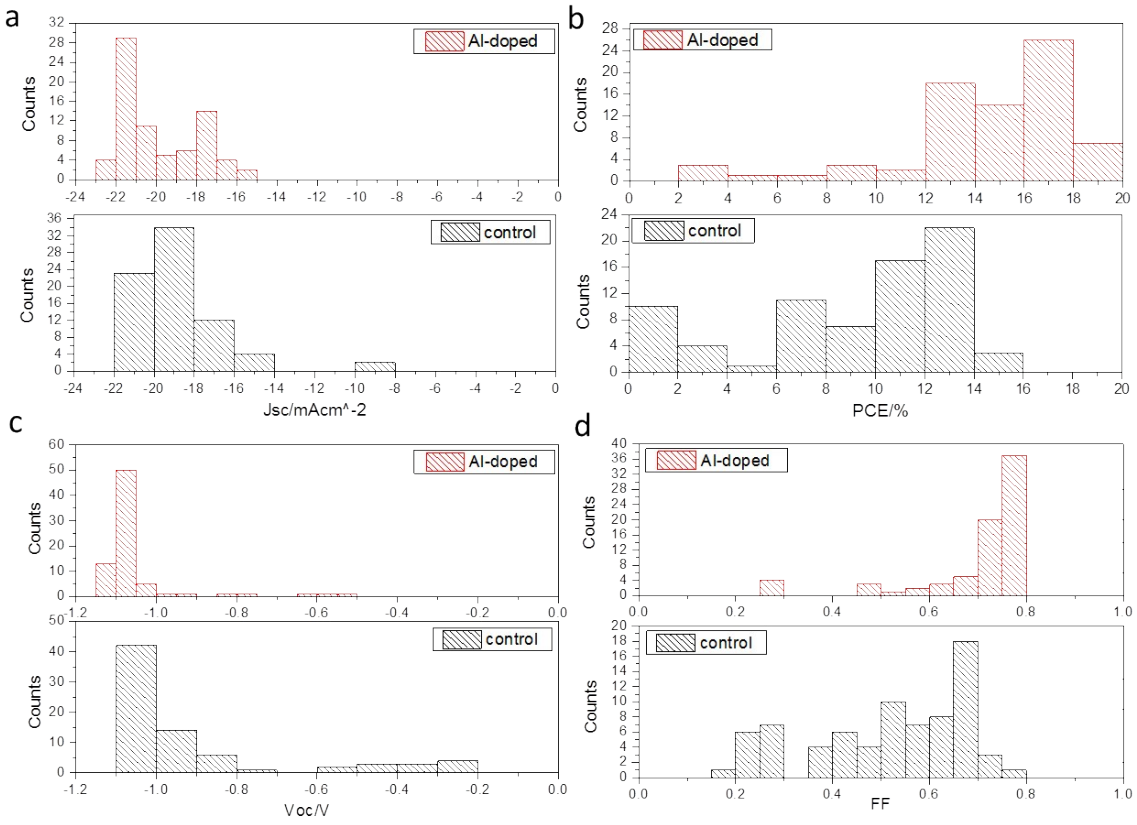

Figure S10. Histograms of the solar cell performance parameters for the optimally doped (0.15 mol%) and control devices.

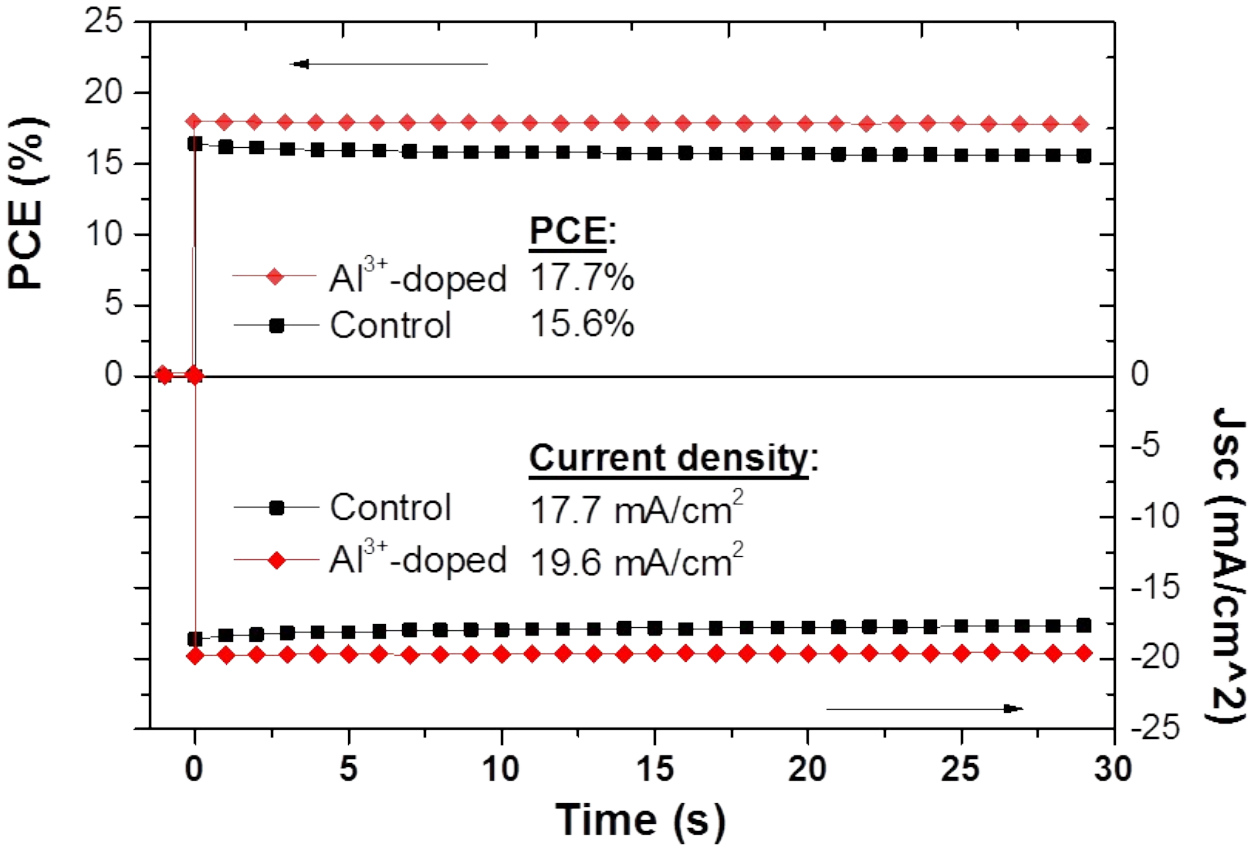

Figure S11. Numerically averaged stabilized power output and photocurrent in a batch of 20 high performing devices of the control and Al^{3+}-doped (0.15 mol%) cells.

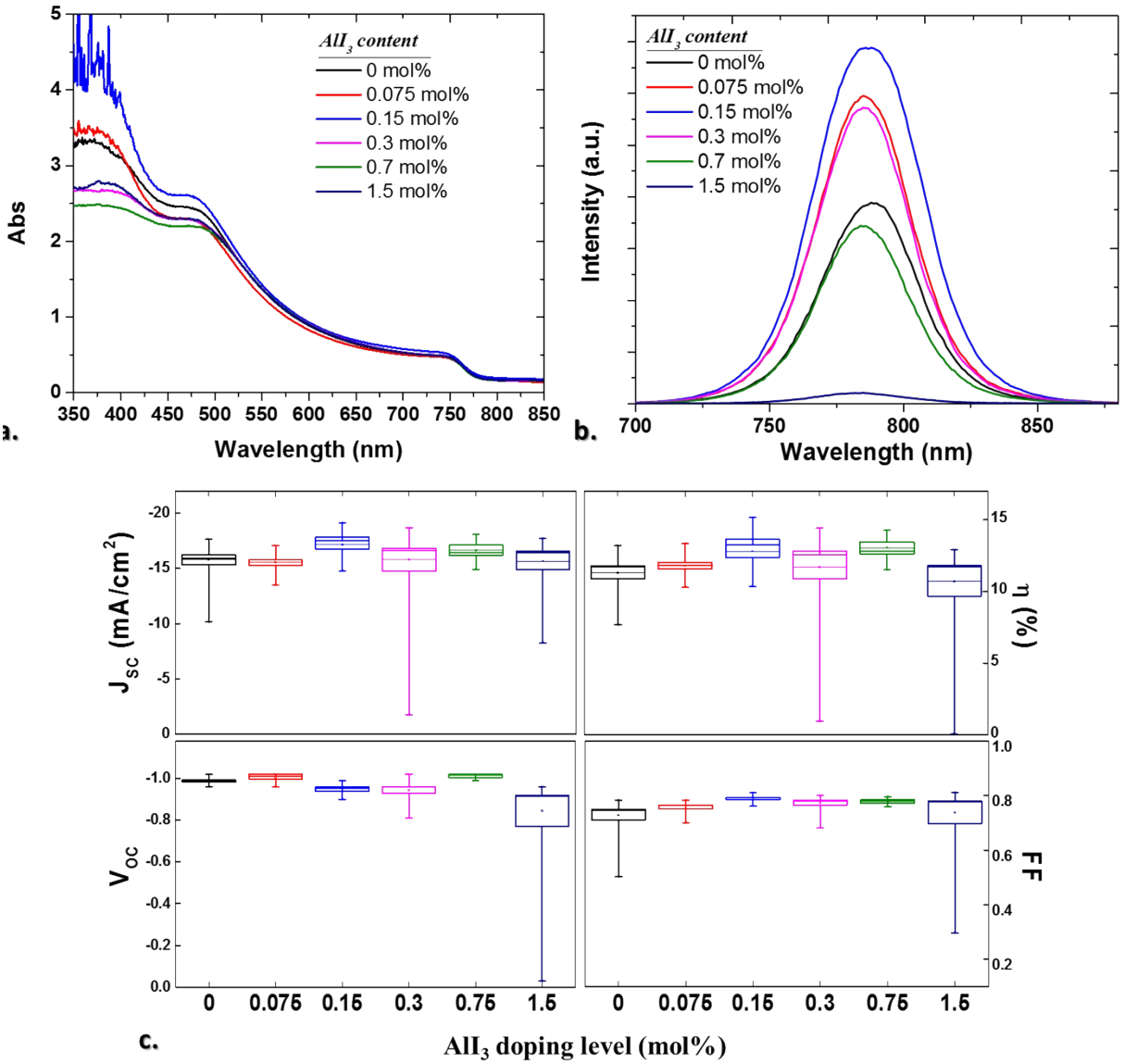

Figure S12. Characterizations of different Al^{3+} doping (AlI_3 as dopant) concentration of perovskite samples with **a)** UV-vis absorption, **b)** spectra Steady-state photoluminescence, **c)** Device performance parameters (with the structure of Ag/BCP/PCBM/perovskite/PEDOT AI4083/FTO) extracted from a batch of current-voltage measurements under simulated AM 1.5, 100 mW/cm^2 irradiance in air. Note: Here we replaced the source of Al^{3+} from Al-acac$_3$ to Aluminum iodide (AlI_3), in this case we substitute the methylammonium iodide for the

corresponding different concentrations of AlI_3 to achieve Al^{3+} doping, while the amount of iodide in the $MAPbI_3$ remains constant.

REFERENCE

1 A. Pramanick, X. P. Wang, C. Hoffmann, S. O. Diallo, M. R. V. Jørgensen and X.-L. Wang, *Phys. Rev. B*, 2015, **92**, 174103.

2 Y. Zhao and J. Zhang, *J. Appl. Crystallogr.*, 2008, **41**, 1095–1108.

3 R. M. Langford and M. Rogers, *Micron*, 2008, **39**, 1325–30.

4 S. D. Stranks, G. E. Eperon, G. Grancini, C. Menelaou, M. J. P. Alcocer, T. Leijtens, L. M. Herz, A. Petrozza and H. J. Snaith, *Science*, 2013, **342**, 341–344.

5 J. C. de Mello, H. F. Wittmann and R. H. Friend, *Adv. Mater.*, 1997, **9**, 230–232.

6 P. G. Schroeder, C. B. France, B. A. Parkinson and R. Schlaf, *J. Appl. Phys.*, 2002, **91**, 9095.

7 J. R. Lindsay, H. J. Rose, W. E. Swartz, P. H. Watts and K. A. Rayburn, *Appl. Spectrosc.*, 1973, **27**, 1–5.

8 A. Hess, E. Kemnitz, A. Lippitz, W. E. S. Unger and D. H. Menz, *J. Catal.*, 1994, **148**, 270–280.

9 A. G. Shard, *Surf. Interface Anal.*, 2014, **46**, 175–185.

10 W. Zhang, S. Pathak, N. Sakai, T. Stergiopoulos, P. K. Nayak, N. K. Noel, A. A. Haghighirad, V. M. Burlakov, D. W. deQuilettes, A. Sadhanala, W. Li, L. Wang, D. S. Ginger, R. H. Friend and H. J. Snaith, *Nat. Commun.*, 2015, **6**, 10030.

11 S. K. Vasheghani Farahani, T. D. Veal, J. J. Mudd, D. O. Scanlon, G. W. Watson, O. Bierwagen, M. E. White, J. S. Speck and C. F. McConville, *Phys. Rev. B*, 2014, **90**, 155413.

12 S. De Wolf, J. Holovsky, S. J. Moon, P. Löper, B. Niesen, M. Ledinsky, F. J. Haug, J. H. Yum and C. Ballif, *J. Phys. Chem. Lett.*, 2014, **5**, 1035–1039.

13 A. Sadhanala, F. Deschler, T. H. Thomas, S. E. Dutton, K. C. Goedel, F. C. Hanusch, M. L. Lai, U. Steiner, T. Bein, P. Docampo, D. Cahen and R. H. Friend, *J. Phys. Chem. Lett.*, 2014, **5**, 2501–2505.

14 S. R. Johnson and T. Tiedje, *J. Appl. Phys.*, 1995, **78**, 5609.

15 A. R. Zanatta and I. Chambouleyron, *Phys. Rev. B*, 1996, **53**, 3833–3836.